

Self-consistent models of cuspy triaxial galaxies with dark matter haloes

R. Capuzzo-Dolcetta

roberto.capuzzodolcetta@uniroma1.it

Dep. of Physics, University of Roma 'La Sapienza', P.le A. Moro 5, I-00185, Roma, Italy

L. Leccese

linda.leccese@uniroma1.it

Dep. of Physics, University of Roma 'La Sapienza', P.le A. Moro 5, I-00185, Roma, Italy

D. Merritt

merritt@astro.rit.edu

*Dep. of Physics, Rochester Inst. of Technology, 84 Lomb Memorial drive, Rochester, NY
14623 - USA*

A. Vicari

alessandrovicari@uniroma1.it

Dep. of Physics, University of Roma 'La Sapienza', P.le A. Moro 5, I-00185, Roma, Italy

ABSTRACT

We have constructed realistic, self-consistent models of triaxial elliptical galaxies embedded in triaxial dark matter haloes. We examined three different models for the shape of the dark matter halo: (i) the same axis ratios as the luminous matter (0.7:0.86:1); (ii) a more prolate shape (0.5:0.66:1); (iii) a more oblate shape (0.7:0.93:1). The models were obtained by means of the standard orbital superposition technique introduced by Schwarzschild. Self-consistent solutions were found in each of the three cases. Chaotic orbits were found to be important in all of the models, and their presence was shown to imply a possible slow evolution of the shapes of the haloes. Our results demonstrate for the first time that triaxial dark matter haloes can co-exist with triaxial galaxies.

Subject headings: galaxies: elliptical and lenticular, cD - galaxies: kinematics and dynamics - methods: numerical

1. Introduction

According to the hierarchical picture of structure formation, galaxies originated from baryons that condensed within dark-matter haloes. If this picture is correct, dark matter should exist within and around galaxies. In the case of spiral galaxies, this has been widely confirmed by the study of rotation curves that remain approximately flat beyond the visible disk, suggesting the presence of invisible matter at large distances from the galactic centre (Rubin 1991). In the case of elliptical galaxies, the general absence of rotating gas disks makes this confirmation more difficult. Giant elliptical galaxies nevertheless show evidence of dark matter via stellar kinematics (Kronawitter et al. 2000), X-ray emission (Mathews & Brighenti 2003), and gravitational lensing (Keeton 2001). Numerical simulations of disk galaxy mergers including dark matter, like the recent work of Dekel et al. (2005), produce elliptical galaxies with stellar kinematics similar to what is observed.

Large-scale simulations of structure formation typically exclude gas and stars, due to the computational complexities associated with gaseous dissipation, radiation, star formation, etc. These simulations make well-defined predictions about the structure of baryon-free dark matter haloes and the dependence of halo properties on mass and formation redshift (Navarro et al. 2004; Diemand, Moore & Stadel 2004).

Much recent work has focussed on the shapes of the haloes (Allgood et al. 2006, Macció et al. 2006; Bett et al. 2006). Simulated haloes are found to be generically prolate/triaxial. The mean short-to-long axis ratio is $0.5 \lesssim \langle c/a \rangle \lesssim 0.7$ and the distribution of c/a is approximately Gaussian, with a sharp cutoff below $c/a \approx 0.3$ that probably reflects the onset of a dynamical bending instability (Merritt & Sellwood 1994). There are indications that mean halo elongation increases with halo mass (Allgood et al. 2006). The shapes of these simulated haloes are apparently supported mainly by anisotropic velocities rather than by figure rotation (Warren et al. 1992).

To the extent that luminous elliptical galaxies formed in a manner analogous to the (simulated) dark-matter haloes – i.e. through dissipationless clustering of smaller galaxies – one expects the structure of the two sorts of system to be similar. Confirmation of this was recently demonstrated in the case of radial density profiles (Merritt et al. 2005a,b): the same fitting function that best describes luminous elliptical galaxies is an equally good description of the N -body haloes. Furthermore the simulated haloes appear to lie on the same relation between surface brightness and size (the “Kormendy relation”) defined by the galaxies (Graham et al. 2006).

With regard to shapes, observations of elliptical galaxies yield only the projected isophotes and so determination of the intrinsic shape distribution requires either statistical analyses

based on large samples (e.g. Ryden 1992, 1996; Tremblay & Merritt 1995, 1996; Ryden, Lauer & Postman 1993; Alam & Ryden 2002; Vincent & Ryden 2005; Plionis, Basilakos & Ragone-Figueroa 2006), or mapping of potentials via detailed kinematical data for individual galaxies (e.g. Franx, Illingworth & de Zeeuw 1991; Statler et al. 2004). Isophotal studies reveal that luminous and faint elliptical galaxies have significantly different shape distributions: the latter have $\langle c/a \rangle \approx 0.75$ while the former are flatter, $\langle c/a \rangle \approx 0.65$ (Tremblay & Merritt 1996). The apparent shape distributions are found to be mildly inconsistent with axial symmetry in the sense that too few, nearly-round galaxies are observed, but these studies do not strongly constrain the degree or distribution of triaxialities. However, detailed kinematical studies of individual galaxies sometimes find evidence for significant triaxiality (Statler et al. 2004).

Still less is known about the true shapes of dark matter haloes, although constraints come from X-ray studies, lensing, and Milky Way kinematics (Tasitsiomi 2003). When comparing such data to the predictions of the N -body models, it is important to keep in mind that halo shapes are likely to be influenced by the presence of the baryons. For instance, if baryonic matter accumulates at the center of the dark-matter potential, the halo is expected to become rounder and less triaxial (Merritt & Quinlan 1998; Springel, White & Hernquist 2004; Kazantzidis et al. 2004).

Given these uncertainties, it is worthwhile to investigate new lines of evidence that might constrain the shapes of dark-matter haloes. Self-consistency studies constitute one such approach, which until now has not been explored. Can stationary, dark-matter haloes of arbitrary shape co-exist with a galaxy, or does the existence of a central, baryonic mass concentration imply restrictions on the elongation or triaxiality of the halo?

In gravitational potentials that respect special symmetries (spherical- or axi-symmetry, for instance), isolating integrals of the motion exist in addition to the energy. Jeans’s (1915) theorem provides a simple prescription for the construction of steady-state phase-space populations in such potentials: the phase-space density must be a function only of the isolating integrals. Orbits in triaxial potentials sometimes respect integrals in addition to the energy (Schwarzschild 1979), but the mathematical form of these integrals is typically unknown. Further, many orbits in triaxial potentials are observed to respect no integrals aside from the energy (Merritt 1980; Valluri & Merritt 1998; Papaphilippou & Laskar 1998).

Jeans’s theorem can be generalized to the non-integrable case: a steady-state galaxy is one in which the phase-space density is constant in every connected region (Kandrup 1998). An example of a connected region is the invariant torus of a regular orbit, or the Arnold web corresponding to the chaotic parts of phase space at a given energy (Tabor 1989; Rasband 1990). However Jeans’s theorem says nothing about how this special state is to

be achieved, and stochastic orbits are often observed to remain confined to subsets of the full allowed region for long periods (e.g. Habib, Kandrup & Mahon 1997), making it unlikely that they would achieve a uniform phase-space population even in a Hubble time.

In the current work, we use the method introduced in 1979 by Schwarzschild for the numerical construction of stationary galaxy models. Schwarzschild’s method was tested on a modified Hubble profile (Schwarzschild 1979) and on a Plummer model (Siopis 1999). Later, it was used by Statler (1987) to demonstrate the self-consistency of model galaxies made of stars distributed according a triaxial density profile with a central core. Subsequently, high resolution observations of HST (Crane et al. 1993; Ferrarese et al. 1994; Lauer et al. 1995) showed that almost all the ellipticals have densities that rise toward the centre approximately as power laws $\rho \sim r^{-\gamma}$, with $\gamma = 2$ for fainter galaxies and $\gamma = 1$ for brighter ones. Merritt & Fridman (1996; hereafter MF96) used Schwarzschild’s method to construct self-consistent solutions galaxy models with both weak and strong cusps. In the case of strong cusps, the large number of stochastic orbits made it more difficult to obtain equilibrium models. Subsequent studies by Merritt (1997), Siopis (1999) and Terzic (2002) confirmed and extended the MF96 results. In these studies, attempts were made to represent the stochastic orbits via fully-mixed, steady-state distributions at each energy.

All the works just cited dealt with galaxies containing a single (luminous) component only. Here, we introduce a second component, the dark matter, presumably consisting of long-lived, “cold,” and collisionless particles, e.g. supersymmetric neutralinos (Bertone, Hooper & Silk 2004).

In the following Section we explain the method – a generalization of Schwarzschild’s – for constructing self-consistent equilibrium models. The details of these models are discussed in Section 3 while in Section 4 we describe their orbital characteristics. In Section 5 our results are analyzed and compared to those of models without dark matter. Finally in Section 6 we discuss the consequences of stochasticity for the long-term stability of the models.

2. Method

In the absence of analytic expressions for the orbital integrals, one must resort to numerical methods to construct self-consistent models of galaxies or dark-matter haloes. To obtain a numerical solution to the problem we follow the Schwarzschild (1979) scheme. The procedure can be summarized as follows:

- (1) A smooth, three-dimensional mass distribution resembling observed galaxies is postulated and the corresponding gravitational potential calculated by means of Poisson’s equa-

tion.

(2) A library of orbits is realized by integration of the equations of motion in this potential starting from a large set of different initial conditions.

(3) The configuration space is divided into cells and the time each orbit spends in any cell is recorded.

(4) A linear combination of these orbits (with non-negative weights) is sought which gives the best discrete approximation to the known masses of the cells.

We generalized Schwarzschild’s method to the construction of two-component (luminous and dark matter), self-consistent models as follows. First, we constructed a catalog of orbits integrating the equations of motion for a particle moving in the potential generated by the sum of the luminous and dark matter density distributions. Then, two different grids of cells, one for the luminous and one for the dark matter components, were built. The technique used to realize each grid is the same described in MF96: the space was first divided by 21 concentric ellipsoidal shells in zones containing an equal amount of one of the two matter components. Then, each octant was divided into three sectors corresponding to

- (i) the volume with $ax > by$ and $ax > cz$,
- (ii) the volume with $by > ax$ and $by > cz$,
- (iii) the volume with $cz > ax$ and $cz > by$.

Finally, we used a set of six planes to divide each sector in 16 regions. In this way, we obtained a total of 1008 cells per octant for each grid. The fraction of time spent by each orbit of this catalog in both sets of cells was recorded. We then used the data for the luminous-matter grid (called *Luminous*) to reproduce, by means of a linear superposition of orbits with non-negative occupation numbers, the given mass of the luminous component in each cell of that grid. The same procedure was followed to reproduce the dark matter distribution on the *Dark matter* grid.

In practice, our optimization problem consisted of minimizing, separately, the quantities

$$\chi_{lum}^2 = \frac{1}{N_{lum}} \sum_{j=1}^{N_{lum}} \left(M_{j;lum} - \sum_{k=1}^{n_{orb}} C_{k;lum} B_{k,j;lum} \right)^2 \quad (1)$$

and

$$\chi_{dm}^2 = \frac{1}{N_{dm}} \sum_{j=1}^{N_{dm}} \left(M_{j;dm} - \sum_{k=1}^{n_{orb}} C_{k;dm} B_{k,j;dm} \right)^2 \quad (2)$$

where $B_{k,j;lum}$ is the fraction of time that the k th orbit spends in the j th cell of the *Luminous* grid and $B_{k,j;dm}$ is the same quantity in the j th cell of the *Dark matter* grid; $M_{j;lum}$ is the mass which the model places in the j th cell of the *Luminous* grid and $M_{j;dm}$ that placed in the j th cell of the *Dark matter* one; $C_{k;lum}$ and $C_{k;dm}$ are the quantities to be determined by the minimization procedure. The latter represent the total mass of stars and dark matter particles, respectively, spread along the k th orbit ($1 \leq k \leq n_{orb}$).

To guarantee non-negative orbital weights, we imposed the constraints $C_{k;lum} \geq 0$ and $C_{k;dm} \geq 0$. The NAG routine E04NCF (Stoer 1971; Gill et al. 1984) was used to solve these constrained least-squares problems.

3. Mass models

3.1. Density and potential

We considered three different mass models for the galaxy+halo system. In each of the three cases, we adopted triaxial shapes for both components but with a different radial distribution for the dark and luminous matter. In the first model the dark matter was assumed to have the same axial ratios as the luminous matter, while the second and third models were characterized by haloes that were more prolate and more oblate, respectively, than the luminous matter.

As in MF96, we adopted the following mass distribution for the luminous component:

$$\rho_l(m) = \frac{M}{2\pi a_l b_l c_l} \frac{1}{m(1+m)^3} \quad (3)$$

with

$$m^2 = \frac{x^2}{a_l^2} + \frac{y^2}{b_l^2} + \frac{z^2}{c_l^2} \quad 0 < c_l < b_l < a_l \quad (4)$$

and M the total luminous mass (see Fig. 1).

For the dark matter component we adopted

$$\rho_{dm}(m') = \frac{\rho_{dm,0}}{(1+m')(1+m'^2)} \quad (5)$$

where

$$m'^2 = \frac{x^2}{a_{dm}^2} + \frac{y^2}{b_{dm}^2} + \frac{z^2}{c_{dm}^2} \quad 0 < c_{dm} < b_{dm} < a_{dm}, \quad (6)$$

and $\rho_{dm,0}$ is the central dark matter density (see Fig. 1).

The density profile in equation (5) was first proposed by Burkert (1995) for the dark matter haloes of dwarf galaxies, and later extended to the whole family of spiral (Salucci & Burkert 2000) and to massive elliptical (Borriello, Salucci & Danese 2003, hereafter BSD) galaxies. By adopting the Burkert profile – which has a large, low-density core – we are favoring data over theory, since N -body simulations of gravitational clustering imply dark-matter densities that increase roughly as a power law inside of the halo virial radius (Navarro, Frenk & White 1996; Moore et al. 1998; Merritt et al. 2005b). Rotation curve studies, on the other hand, are generally interpreted as implying low ($\sim (1 - 5) \times 10^{-2} M_{\odot} \text{pc}^{-3}$) dark matter densities within the region ($r < 10^2$ pc) where the rotation curves are sampled (e.g. Burkert 1995; Salucci & Burkert 2000; de Blok & Bosma 2002; Gentile et al. 2005). It was to model these low observed dark matter densities that the Burkert model (5) was postulated.

At large radii, the Burkert profile is similar to the NFW and Moore profiles that are commonly fit to N -body haloes, i.e. $\rho_{dm} \propto r^{-3}$. In the central regions where the two sorts of profile (core vs. power law) differ, the gravitational potential is dominated by the luminous galaxy. Thus, our conclusions about the constraints that a central galaxy places on the shape of the halo are probably applicable also to halo models without cores.

The gravitational potential at a point $\mathbf{x} = (x, y, z)$ due to a mass distribution $\rho = \rho(w)$, where $w^2 = x^2/a^2 + y^2/b^2 + z^2/c^2$ may be written (Chandrasekhar 1969)

$$\Phi(\mathbf{x}) = -\pi Gabc \int_0^{\infty} \frac{[\Psi(\infty) - \Psi(w)]d\tau}{\sqrt{(\tau + a^2)(\tau + b^2)(\tau + c^2)}} \quad (7)$$

with

$$\Psi(w) = 2 \int_0^w w' \rho(w') dw' \quad (8)$$

and

$$w^2(\tau) = \frac{x^2}{a^2 + \tau} + \frac{y^2}{b^2 + \tau} + \frac{z^2}{c^2 + \tau}. \quad (9)$$

Consequently, we find, for the luminous and dark matter potentials, respectively,

$$\Phi_l(\mathbf{x}) = -\frac{GM}{2} \int_0^{\infty} \frac{d\tau}{\Delta} \frac{1}{(1+m)^2}, \quad (10)$$

$$\begin{aligned} \Phi_{dm}(\mathbf{x}) = & -\pi G a_{dm} b_{dm} c_{dm} \rho_{dm,0} \\ & \times \int_0^{\infty} \frac{d\tau}{\Delta'} \left[\frac{\pi}{2} - \arctan m' + \log(1+m') - \frac{1}{2} \log(1+m'^2) \right], \end{aligned} \quad (11)$$

with

$$\Delta = \sqrt{(\tau + a_l^2)(\tau + b_l^2)(\tau + c_l^2)} \quad (12)$$

and

$$\Delta' = \sqrt{(\tau + a_{dm}^2)(\tau + b_{dm}^2)(\tau + c_{dm}^2)}. \quad (13)$$

The components of the gravitational forces are

$$F_{l_i} = -\frac{\partial\Phi_l}{\partial x_i} = -GMx_i \int_0^\infty \frac{d\tau}{\Delta(a_i^2 + \tau)(1+m)^3m} \quad (14)$$

$$F_{dm_i} = -\frac{\partial\Phi_{dm}}{\partial x_i} = -2\pi G a_{dm} b_{dm} c_{dm} \rho_{dm,0} x_i \times \int_0^\infty \frac{d\tau}{\Delta'(a_i'^2 + \tau)(1+m')(1+m'^2)} \quad (15)$$

with $a_1 = a_l$, $a_2 = b_l$, $a_3 = c_l$, $a'_1 = a_{dm}$, $a'_2 = b_{dm}$, $a'_3 = c_{dm}$ and $i = 1, 2, 3$. These integrals were rewritten using an appropriate change of variables (see Appendix A) in order to reduce the complexity of their numerical treatment.

The mass contained in the ellipsoid of semi-axes wa , wb and wc is

$$M(w) = 4\pi abc \int_0^w \rho(w')w'^2 dw'; \quad (16)$$

this implies that the total mass is $M_{tot} = \lim_{w \rightarrow \infty} M(w)$. In the case of luminous and dark matter, respectively, equation (16) gives (see Fig. 1):

$$M_l(m) = M \left(\frac{m}{1+m} \right)^2, \quad (17)$$

$$M_{dm}(m') = \pi a_{dm} b_{dm} c_{dm} \rho_{dm,0} B(m'), \quad (18)$$

where B is the function

$$B(m') = -2\text{atan}(m') + 2 \log(1+m') + \log(1+m'^2). \quad (19)$$

We note that the total mass of the dark matter model is infinite. We cut off the dark matter grid at $m = m'_{max}$, where $m'_{max} \approx 19$ was determined by the requirement that the mass in dark matter was ten times greater than the luminous total mass.

3.2. Model parameters and constraints

The free parameters of our models are:

- a_l , b_l , c_l and M for the luminous component;

- a_{dm} , b_{dm} , c_{dm} and $\rho_{dm,0}$ for the dark matter.

With regard to the axis ratios of the luminous component, there exist some constraints in the form of the observed distribution of galaxy isophotal shapes (Ryden 1992; Tremblay & Merritt 1995, 1996; Alam & Ryden 2002; Plionis, Basilakos & Ragono-Figueroa 2006). Intrinsic, short-to-long axis ratios of bright ($M_B < -20$) elliptical galaxies appear to be narrowly clustered around 3/4 (Tremblay & Merritt 1996); the constraints on the second axis ratio are less strong, but most studies (e.g. Tremblay & Merritt 1995) find that axisymmetric shapes can be securely ruled out. We accordingly fixed the short-to-long axis ratio of the luminous component to be 0.7 in all of the models and assumed “maximal triaxiality,” i.e.

$$\frac{c_l}{a_l} = 0.7, \quad T \equiv \frac{a_l^2 - b_l^2}{a_l^2 - c_l^2} = \frac{1}{2}. \quad (20)$$

For the dark matter, we investigated three choices for the axis ratios: equal to those of the luminous matter (MOD1); a more prolate shape ($T = 0.75$) with $c_{dm}/a_{dm} = 0.5$ (MOD2); and a more oblate shape ($T = 0.25$) with $c_{dm}/a_{dm} = 0.7$ (MOD3) The parameters of the models are summarized in Table 1.

If the unit of length is taken to be a_l , there remain two parameters: the ratio of luminous to dark-matter scale lengths and the normalization of the dark matter density.

We applied the results of the fundamental plane study of Borriello, Salucci & Danese (2003) to the triaxial case, yielding $a_{dm}/a_l = 3.64$ and the value of $\rho_{dm,0}$ corresponding to

$$\Gamma_e \equiv \frac{M_{dm}(m'_e)}{M_l(m_e)} \simeq 0.3 \quad (21)$$

which is obtained by the evaluation of the luminous matter within the ellipsoid delimited by m_e , that characterizes the ‘luminous’ ellipsoid having the x -semiaxis equal to the effective

TABLE 1

MODEL	Luminous matter		Dark matter	
	c_l/a_l	T_l	c_{dm}/a_{dm}	T_{dm}
MOD1	0.7	0.5	0.7	0.5
MOD2	0.7	0.5	0.5	0.75
MOD3	0.7	0.5	0.7	0.25

Table 1: Axial ratios and triaxial parameter of the density distributions of the 3 galactic models.

radius $R_e = 1.81a_l$ (m_e is the triaxial generalization of the effective radius R_e), and that of the dark matter contained in the $m'_e = 0.5$ ellipsoid having the same long-axis extension as the luminous one. According to BSD this $(a_{dm}/a_l, \Gamma_e)$ pair of values gives the best fit of theoretical data to the FP. From this constraint it follows that $\rho_{dm,0} = 1.26 \times 10^{-2} M_{l,T}/a_l^3$ for MOD1, $\rho_{dm,0} = 2.26 \times 10^{-2} M_{l,T}/a_l^3$ for MOD2 and $\rho_{dm,0} = 1.14 \times 10^{-2} M_{l,T}/a_l^3$ for MOD3.

Hereafter we express all quantities in units such that G , a_l and M are equal to unity. The implied unit of time is

$$T_u = G^{-1/2} a_l^{3/2} M^{-1/2} = 1.49 \times 10^6 \text{yr} \left(\frac{M}{10^{11} M_\odot} \right)^{-1/2} \left(\frac{a_l}{1 \text{kpc}} \right)^{3/2} \quad (22)$$

and $V_u = \sqrt{GM/a_l}$ is the unit of velocity; the, derived, energy unit is $E_u = (GM^2/a_l)$.

4. Orbital catalogs

4.1. Initial conditions

The orbital catalogs were built as in Schwarzschild (1993). Initial conditions consisted either of zero initial velocity (“stationary” start-space), or points in the $X - Z$ plane with $v_x = v_z = 0$ and $v_y = \sqrt{2(E - \Phi)} \neq 0$ ($X - Z$ start-space). As argued by Schwarzschild (1993), these choices cover most of the orbital types in the full phase space of a nonrotating triaxial model; in particular, orbits starting in the $X - Z$ plane are mostly tubes and avoid a region around the center of the model, while orbits starting on an equipotential surface are either stochastic or regular boxlets, that approach the origin after a sufficiently long time. For each galactic model we fixed 32 energy values and for each value we selected a set of 150 initial conditions from the $X - Z$ start-space and a set of 192 initial conditions from the stationary start-space, thus obtaining a catalog of 10944 orbits. Each orbit was integrated in time using a 7/8 order Runge-Kutta-Fehlberg algorithm with a variable step size so as to have a relative error in energy less than 10^{-6} per time step.

4.2. Integration times

Particular care must be given to the choice of the orbital integration time. Because our aim is to construct a stationary model of a galaxy, all orbits must be integrated over a time interval long enough to guarantee a steady-state galaxy model. This means that the occupation numbers $B_{k,j}$ of each orbit in the grid cells must be time-invariant. The

time required by the $B_{k,j}$ to converge to stationary values varies from one orbit to another, whether the orbit is regular or stochastic. In fact, a regular orbit can fill its invariant torus in a short time or, in the case of a nearly resonant orbit, it can take much longer to fill it (Merritt & Valluri 1999). In the same way, some chaotic orbits diffuse rapidly in the entire phase-space permitted by their energy, while others remain confined between regular tori for a very long time (Valluri & Merritt 2000) (we will call *ergodic* the orbits with convergent $B_{k,j}$).

To select the integration time for the orbits we followed an iterative procedure, proposed by Pfenniger (1984), that stops the integration when the relative variations of $B_{k,j;lum}$ and $B_{k,j;dm}$, in a time step go below 0.5%. In detail, we proceeded as follows:

- 1) Integrate and store the $B_{k,j;lum}$ and $B_{k,j;dm}$ over a time $\tau = T_d/2$ where T_d is the “dynamical time,” defined for each given energy as the period of the 1 : 1 resonant orbit in the $X - Y$ plane (see MF96);
- 2) Restart the integration for another time τ , and store the new $B_{k,j;lum}$ and $B_{k,j;dm}$ at the end;
- 3) Compare the new and old $B_{k,j;lum}$ and $B_{k,j;dm}$. If the maximum relative difference is greater than 0.005 then average the two sets of $B_{k,j;lum}$ and $B_{k,j;dm}$, double τ and repeat step 2, otherwise stop the computation.

As argued by Pfenniger, this method does not converge for all orbits (e.g. “sticky” chaotic orbits), so it is needed to fix a maximum time of integration, t_{max} .

We set this value at $t_{max} = 2T_H$, where T_H is the Hubble time; the choice $T_H = 15Gyr$ means $t_{max} = 10,000T_u$, where T_u is the time unit in eq. 22 once assumed $M = 10^{11} M_\odot$ and $a_l = 1kpc$.

Most of the CPU time was associated with the integration of the orbit libraries. Since each orbit is independent, this task is efficiently parallelized. We used the Plexus cluster at the Rochester Institute of Technology to carry out the integrations. The construction of the complete library of 10944 orbits for MOD1 required approximately 6 hours using in parallel 16 nodes of the cluster.

5. Results

5.1. Self-consistency

The main result of this work is that we were able to successfully construct self-consistent models in all of the cases considered for the shape of the DM halo. To obtain the model with the prolate shape of the dark matter distribution (MOD3) we needed to enlarge the catalog of orbits to 11970. For each matter component, a parameter, δ , indicating the departure from self-consistency may be defined as

$$\delta = \frac{\sqrt{\chi^2}}{\overline{M}} \quad (23)$$

where \overline{M} represents the average mass contained in the grid cells and χ^2 is the quantity defined in Section 2. The dependence of δ on the choice of the number of orbits in the catalog is shown in Fig. 2 for MOD2; Fig. 3 gives the distribution of the relative error in mass, ϵ , defined as $\epsilon = |M_j - \sum_{k=1}^{n_{orb}} C_k B_{k,j}|/M_j$ for each j 'th grid cell in each of the three self-consistent models.

If we analyze the orbits that contribute significantly to the self-consistent solutions, we find that a large fraction consist of orbits that do not conserve the sign of the components of the angular momentum (corresponding to regular box orbits and boxlets or to chaotic orbits). Regarding orbits that conserve the z - component (named short-axis tubes) or the x - component (outer tubes) of the angular momentum, it is noted that, to guarantee the prolate structure of the dark matter in MOD2, the fraction of outer orbits was greater than that of the short tubes, while the opposite was true in MOD3, the more oblate model.

To give a finer detail on the self-consistent model orbital structure, Fig. 4 and 5 show the cumulative contribution, by mass, of the various orbital families in our self-consistent solutions. Chaotic orbits are of increasing importance at higher energies, especially for the dark matter component. This is partly explained by the initial abundance of high energy chaotic orbits in the full MOD1 catalog (see Fig. 6). Fig. 6 indicates, also, how the low-energy back-bone of the self consistent model is mostly constituted by short-axis tube orbits; in the "more" evolved MOD1bis model (described in more detail below), chaotic orbits of the luminous matter component are important on the whole energy range. All this suggests to investigate more deeply the role of orbital stochasticity, as we do in Sect. 6.

5.2. Velocity dispersion tensors

To gain a more complete picture of the model kinematics, we also evaluated the first and second velocity moments in each of the self-consistent solutions. Using the properties of symmetry with respect to the coordinate planes in the cartesian frame, it was sufficient to store data for any given orbit in only one of the eight octants.

We stored the velocities along an orbit symmetrizing them respect to the principal axes in order to insert the point in which one velocity is evaluated in a precise cell of the positive octant. In this way an orbit, starting with a fixed direction, correspond to a trajectory covered equally (or similar) in two opposite directions. It results a mean motions in each cell near to the zero value. Then we weighted these data with the occupation number (mass) of the luminous orbits in each cell obtaining:

$$\langle V_i \rangle_{lum} = \frac{\sum_{k=1}^{n_{orbit}} C_{k;lum} B_{k,j;lum} \langle v_i \rangle_{lum}}{\sum_{k=1}^{n_{orbit}} C_{k;lum} B_{k,j;lum}}$$

and

$$\langle V_i V_h \rangle_{lum} = \frac{\sum_{k=1}^{n_{orbit}} C_{k;lum} B_{k,j;lum} \langle v_i v_h \rangle_{lum}}{\sum_{k=1}^{n_{orbit}} C_{k;lum} B_{k,j;lum}}.$$

Finally, we obtain the velocity dispersion tensor of the stars, $\sigma_{lum,ih}^2$ in each cell l , as:

$$\sigma_{lum,l;ih}^2 = \langle V_i V_h \rangle_{lum,l} - \langle V_i \rangle_{lum,l} \langle V_h \rangle_{lum,l}.$$

The diagonalization of the velocity dispersion tensor, leads to the three principal velocity dispersions, $\sigma_{lum,l;i}^2$ ($i = 1, 2, 3$) having the profiles shown in the left column of Fig. 7 (we order the dispersions to have $\sigma_{lum,l;1}^2 > \sigma_{lum,l;2}^2 > \sigma_{lum,l;3}^2$). In the right column of the figure we show, for comparison, the corresponding principal dispersions evaluated in a model with only the luminous component. As expected, the velocity dispersion in the model with both luminous and dark matter have a flatter profile. The difference in the external region is mainly due to insufficient orbital sampling and the (necessary) cut-off in the dark matter distribution.

6. Importance of orbital stochasticity

The Schwarzschild method for building self-consistent models uses orbits as “templates”, with supposedly time-invariant properties, so a requirement for a stationary solution is that a large fraction of the orbits (whether regular or chaotic) have nearly time-independent occupation numbers. Using the method of Pfenniger discussed above, we found that, at

the time $2T_H$, roughly 20% of the occupation numbers of the orbits used to represent the luminous component were not yet fixed in time, while for the dark matter this percentage was as high as $\sim 50\%$. For MOD1, we attempted to obtain a more “stationary” solution by integrating the orbits up to $5T_H$. In this way, using a total of 2851 orbits for the luminous component and 2796 for the dark matter, we achieved a solution (MOD1bis) with a relative error in the mass of each cell $< 10^{-9}$ (see Fig. 8). In this new model, the number of orbits with non-steady $B_{k,j}$ values was reduced to $\sim 15\%$, which would seem to indicate the presence in the initial solution of quite a few “sticky” chaotic orbits.

Evaluating stochasticity based on orbital occupation numbers is prone to error, since even regular orbits can take long times to fill their invariant tori. To more accurately identify stochastic orbits, we used the Smaller Alignment Index (SALI) introduced by Skokos (2001), and later applied successfully to different dynamical systems (Skokos et al. 2003; Skokos et al. 2004; Manos & Athanassoula 2006). It is defined as (Skokos 2001)

$$SALI(t) = \min \left\{ \left\| \frac{\mathbf{w}_1(t)}{\|\mathbf{w}_1(t)\|} + \frac{\mathbf{w}_2(t)}{\|\mathbf{w}_2(t)\|} \right\|, \left\| \frac{\mathbf{w}_1(t)}{\|\mathbf{w}_1(t)\|} - \frac{\mathbf{w}_2(t)}{\|\mathbf{w}_2(t)\|} \right\| \right\}$$

where $\mathbf{w}_1(t)$ and $\mathbf{w}_2(t)$ are two deviation vectors in phase space, centered in the initial condition of one orbit and pointing in two different arbitrary directions. In the case of Hamiltonian flows, SALI fluctuates around a non-zero value for regular orbits, while it tends (in time) to zero for chaotic orbits.

By studying the evolution of this quantity for all the orbits of the catalog used to seek for the self-consistent solution of MOD1 we found that 68% of them are chaotic, especially at high energies (see Fig. 9). Regarding the orbits of the subsample giving the self-consistent solution MOD1bis, we found that more than 90% of non ergodic orbits are chaotic.

To evaluate the degree to which the stochastic orbits in MOD1bis would cause this model to evolve over long periods, we recorded the position and velocity of every chaotic orbit at the end ($t = 5T_H$) of the integration and used these values as initial conditions for a new

TABLE 2

Set	Luminous matter		Dark matter	
	$\langle w \rangle$	$\sigma_{\langle w \rangle}$	$\langle w \rangle$	$\sigma_{\langle w \rangle}$
X	0.000872	0.00138	0.00388	0.00137
Y	-0.00845	0.00150	-0.01	0.00165
Z	0.00929	0.00177	0.00771	0.00157

Table 2: The mean values of the “evolution” parameter w and their standard deviations.

integration over another T_H . We then again recorded the occupation numbers and compared them with the old ones. As shown in Fig. 10, more than 90% of these “reintegrated” orbits have fluctuations in $B_{i,j}$ greater than the canonical value of 0.005. Operating in a similar way for dark matter, we reached the conclusion that our self-consistent model contains $\sim 10\%$ and $\sim 23\%$ of still-evolving stellar and dark matter orbits, respectively.

In order to study the cell density change as a result of orbital evolution, and so the role of evolution on the overall shape of the model galaxy, we studied the variation of the occupation numbers of the chaotic-non ergodic orbits on a $T_H - 5T_H$ time basis, of three set of cells (named X, Y, Z), sampling the volumes around the three coordinate axes. At this scope we defined, in each cell (i), an “evolution” parameter

$$w_i = \frac{\sum_{k \in K1} B_{i,k}|_{5th} - \sum_{k \in K1} B_{i,k}|_{1th}}{\sum_{k \in K2} B_{i,k}|_{5th}} \quad (24)$$

where in the numerator summation is extended over all the chaotic-non ergodic orbits in the self-consistent solutions and, to normalize, we divide for the sum over the whole set of orbits in the self-consistent solution at $t = 5T_H$. The average value of w on the X, Y, Z volumes gives an indication of the shape evolution: a globally unchanged shape would correspond to $\langle w \rangle_X = \langle w \rangle_Y = \langle w \rangle_Z = 0$. We found that for luminous matter $\langle w \rangle_X$ is compatible with being = 0, while $\langle w \rangle_Y < 0$ and, $\langle w \rangle_Z > 0$. This corresponds to a slight evolution toward a more prolate shape. The dark matter component shows a, statistically significant, increase in time of the chaotic orbit population of both the X and Z volumes, and a (smaller) depopulation of the Y volume. This should corresponds, too, toward a more prolate configuration. In view of future astrophysical applications (e.g. to the study of orbital the evolution of massive black holes or globular clusters subjected to dynamical friction), it is relevant to check how much the kinematical structure of the galactic models depend on the presence of a fraction of evolving orbits. To do this, we compared the principal velocity dispersions in MOD1bis with those of MOD1. As we can see by comparing Fig. 11 with Fig. 7, the behaviours are similar, with a relative difference that is almost always below 10%. We checked that the largest relative differences refer to the outermost shell.

Acknowledgments

D.M. acknowledges support from grants AST-0206031, AST-0420920 and AST-0437519 from the NSF, grant NNG04GJ48G from NASA, and grant HST-AR-09519.01-A from STScI. This work was supported in part by the Center for Advancing the Study of Cyberinfrastructure at the Rochester Institute of Technology.

A. Potential and forces

Using the substitution $s = (1 + \tau)^{-1/2}$ in Eq. 10 and 11, they transforms into:

$$\Phi_l(\mathbf{x}) = -GM \int_0^1 \frac{ds}{\Delta'} \left[\frac{1}{(1+m)^2} \right] \quad (\text{A1})$$

$$\begin{aligned} \Phi_{dm}(\mathbf{x}) &= -2\pi G a_{dm} b_{dm} c_{dm} \rho_{dm,0} \\ &\times \int_0^1 \frac{ds}{\Delta'} \left(\frac{\pi}{2} - a \tan m' + \log(1+m') - \frac{1}{2} \log(1+m'^2) \right), \end{aligned} \quad (\text{A2})$$

where

$$m^2(s) = s^2 \left[\frac{x^2}{1+s^2(a_l^2-1)} + \frac{y^2}{1+s^2(b_l^2-1)} + \frac{z^2}{1+s^2(c_l^2-1)} \right] \quad (\text{A3})$$

$$\tilde{\Delta} = \sqrt{[1+s^2(a_l^2-1)][1+s^2(b_l^2-1)][1+s^2(c_l^2-1)]}$$

and

$$m'^2(s) = s^2 \left[\frac{x^2}{1+s^2(a_{dm}^2-1)} + \frac{y^2}{1+s^2(b_{dm}^2-1)} + \frac{z^2}{1+s^2(c_{dm}^2-1)} \right] \quad (\text{A4})$$

$$\tilde{\Delta}' = \sqrt{[1+s^2(a_{dm}^2-1)][1+s^2(b_{dm}^2-1)][1+s^2(c_{dm}^2-1)]}$$

With the substitutions $s = a_{l;i}(a_{l;i}^2 + \tau)^{-1/2}$ for the luminous forces and $s = a_{dm;i}(a_{dm;i}^2 + \tau)^{-1/2}$ for that of dark matter we transform Eq. 14 and 15 in:

$$F_{l_i} = -GM \frac{\partial \Phi_l}{\partial x_i} = -2x_i \int_0^1 \frac{s^2 ds}{\Delta_i m_i (1+m_i)^3} \quad (\text{A5})$$

$$\begin{aligned} F_{dm_i} &= -\frac{\partial \Phi}{\partial x_i} = -4\pi G a_{dm} b_{dm} c_{dm} \rho_{dm,0} x_i \\ &\times \int_0^1 \frac{s^2 ds}{\Delta'_i (1+m'_i)(1+m_i'^2)} \end{aligned} \quad (\text{A6})$$

where $x_1 = x$, $x_2 = y$, $x_3 = z$ and:

$$\begin{aligned}
 m_i^2(s) &= s^2 \left[\frac{x^2}{a_{l,i}^2 + C_{l,1}s^2} + \frac{y^2}{a_{l,i}^2 + C_{l,2}s^2} + \frac{z^2}{a_{l,i}^2 + C_{l,3}s^2} \right] \\
 m_i'^2(s) &= s^2 \left[\frac{x^2}{a_{dm,i}^2 + C_{dm,1}s^2} + \frac{y^2}{a_{dm,i}^2 + C_{dm,2}s^2} + \frac{z^2}{a_{dm,i}^2 + C_{dm,3}s^2} \right] \\
 \Delta_i &= \sqrt{(a_{l,i}^2 + A_{l,1}s^2)(a_{l,i}^2 + A_{l,2}s^2)(a_{l,i}^2 + A_{l,3}s^2)} \\
 \Delta_i' &= \sqrt{(a_{dm,i}^2 + A_{dm,1}s^2)(a_{dm,i}^2 + A_{dm,2}s^2)(a_{dm,i}^2 + A_{dm,3}s^2)}.
 \end{aligned} \tag{A7}$$

The constants in Eq. A7 are

$$\begin{aligned}
 i = 1 : \\
 A_{j;1} &= b_j^2 - 1 & A_{j;2} &= c_j^2 - 1 & A_{j;3} &= a_j^2 \\
 C_{j;1} &= 0 & C_{j;2} &= b_j^2 - 1 & C_{j;3} &= c_j^2 - 1 \\
 i = 2 : \\
 A_{j;1} &= c_j^2 - b_j^2 & A_{j;2} &= 1 - b_j^2 & A_{j;3} &= b_j^2 \\
 C_{j;1} &= 1 - b_j^2 & C_{j;2} &= 0 & C_{j;3} &= c_j^2 - b_j^2 \\
 i = 3 : \\
 A_{j;1} &= 1 - c_j^2 & A_{j;2} &= b_j^2 - c_j^2 & A_{j;3} &= c_j^2 \\
 C_{j;1} &= 1 - c_j^2 & C_{j;2} &= b_j^2 - c_j^2 & C_{j;3} &= 0.
 \end{aligned} \tag{A8}$$

with $j = l$ or $j = dm$ if we deal with luminous or dark matter, respectively.

REFERENCES

- Alam, S. M. K., & Ryden, B. S. 2002, ApJ, 570, 610
- Allgood, B., Flores, R. A., Primack, J. R., Kravtsov, A. V., Wechsler, R. H., Faltenbacher, A., & Bullock, J. S. 2006, MNRAS, 367, 1781
- Bertone, G., Hooper, D., & Silk, J. 2004, Physics Reports, 405, 279
- Bett, P., Eke, V., Frenk, C. S., Jenkins, A., Helly, J., & Navarro, J. 2006, ArXiv Astrophysics e-prints, arXiv:astro-ph/0608607
- Borriello A., Salucci P., Danese L. 2003, MNRAS, 341, 1109
- Burkert A. 1995, ApJ, 447, L25

- Chandrasekhar S. 1969, *Ellipsoidal Figures of Equilibrium* (New York:Dover)
- Cole S., Lacey C. 1996, *MNRAS*, 281, 716
- Crane, P. et al. 1993, *AJ*, 106, 1371
- de Blok, W. J. G., & Bosma, A. 2002, *A&A*, 385, 816
- Dekel F., Stoehr F., Mamon G.A., Cox T.J., Novak G.S., Primack J.R. 2005, *Nature*, 437, 707
- Diemand, J., Moore, B., & Stadel, J. 2004, *MNRAS*, 353, 624
- Faber S.M., Tremaine S., Ajhar E.A., Byun Y.-I., Dressler A., Gebhardt K., Grillmair C., Kormendy J., Lauer T.R., Richstone D. 1997, *AJ*, 114, 1771
- Franx, M., Illingworth, G., & de Zeeuw, T. 1991, *ApJ*, 383, 112
- Ferrarese L., van den Bosch F.C., Ford H.C., Jaffe W., O’Connell R. W. 1994,*AJ*, 108, 1598
- Gentile, G., Burkert, A., Salucci, P., Klein, U., & Walter, F. 2005, *ApJl*, 634, L145
- Gill P. E. et al. 1984, *ACM Trans. Math. Software*, 10, 282
- Habib, S., Kandrup, H. E., & Mahon, M. E. 1997, *ApJ*, 480, 155
- Jeans, J. H. 1915, *MNRAS*, 76, 70
- Kandrup, H. E. 1998, *MNRAS*, 299, 1139
- Kazantzidis, S., Kravtsov, A. V., Zentner, A. R., Allgood, B., Nagai, D., & Moore, B. 2004, *ApJl*, 611, L73
- Keeton C.R. 2001, *ApJ*, 561, 46
- Kronawitter, A., Saglia, R. P., Gerhard, O., & Bender, R. 2000, *A & Ap. Suppl.*, 144, 53
- Lauer T.R., Ajhar E.A., Byun Y.-I., Dressler A., Faber S.M., Grillmair C., Kormendy J., Richstone D., Tremaine, S 1995, *AJ*, 110, 2622
- Maccio’, A. V., Dutton, A. A., van den Bosch, F. C., Moore, B., Potter, D., & Stadel, J. 2006, *ArXiv Astrophysics e-prints*, arXiv:astro-ph/0608157
- Manos T., Athanassoula E. 2006, *astro-ph/0601331 v1*
- Mathews W.G., Brighenti F. 2003, *Ann. Rev. Astron. Astrophys.*, 41, 191

- Merritt, D. 1980, *ApJ Suppl.*, 43, 435
- Merritt, D. 1997, *Apj*, 486, 102
- Merritt D., Fridman T. 1996, *ApJ*, 460, 136
- Merritt, D., Graham, A. W., Moore, B., Diemand, J., & Terzic, B. 2005b, *ArXiv Astrophysics e-prints*, arXiv:astro-ph/0509417
- Merritt, D., Navarro, J. F., Ludlow, A., & Jenkins, A. 2005a, *ApJl*, 624, L85
- Merritt, D., & Valluri, M. 1999, *AJ*, 118, 1177
- Moore, B., Governato, F., Quinn, T., Stadel, J., & Lake, G. 1998, *ApJl*, 499, L5
- Moore B., Kazantzidis S., Diemand J., Stadel J. 2004, *MNRAS*, 354, 522
- Navarro, J. F., Frenk, C. S., & White, S. D. M. 1996, *ApJ*, 462, 563
- Ostriker J.P., Steinhardt P. 2003, *Science*, 300
- Papaphilippou, Y., & Laskar, J. 1998, *A & A*, 329, 451
- Pfenniger D. 1984, *ApJ*, 141, 171
- Plionis, M., Basilakos, S., & Ragone-Figueroa, C. 2006, *ArXiv Astrophysics e-prints*, arXiv:astro-ph/0608457
- Rasband S. N. 1990, “Arnold diffusion” in *Chaotic Dynamics of Nonlinear Systems* (New York, Wiley)
- Rubin, V. C. 1991, *AIP Conf. Proc.* 222: After the first three minutes, 222, 371
- Ryden, B. 1992, *ApJ*, 396, 445
- Ryden, B. S. 1996, *ApJ*, 461, 146
- Ryden, B. S., Lauer, T. R., & Postman, M. 1993, *ApJ*, 410, 515
- Salucci P., Burkert A. 2000, *Apj*, 537, 9
- Schwarzschild M. 1979, *ApJ*, 232, 236
- Schwarzschild M. 1993, *ApJ*, 409, 563
- Siopis Ch. 1999, *ASPC*, 182, 176

- Skokos Ch. 2001, *J. Phys. A: Math. Gen.*, 34, 10029
- Skokos Ch., Antonoupolos C., Bountis T., Vrahatis M. 2003, *Prog. Theor. Phys. Suppl.*, 150, 439
- Skokos Ch., Antonoupolos C., Bountis T., Vrahatis M. 2004, *J. Phys. A*, 37, 6269
- Springel, V., White, S. D. M., & Hernquist, L. 2004, *IAU Symposium*, 220, 421
- Statler Thomas S. 1987, *Apj*, 321, 113
- Statler, T. S., Emsellem, E., Peletier, R. F., & Bacon, R. 2004, *MNRAS*, 353, 1
- Stiavelli M., Miller B.W., Ferguson H.C., Mack J., Whitmore B.C., Lotz J.M. 2001, *AJ*, 121, 1385
- Stoer J. 1971, *SIAM Numer. Anal.*, 8, 382
- Tabor M. 1989, *Chaos and integrability in nonlinear dynamics. An introduction.* (New York, Wiley)
- Tasitsiomi, A. 2003, *International Journal of Modern Physics D*, 12, 1157
- Terzić, B. 2002, Ph.D. Thesis, University of Florida
- Tremblay, B. & Merritt, D. 1995, *AJ*, 110, 1039
- Tremblay B. & Merritt, D. 1996, *AJ*, 111, 2243
- Valluri, M., & Merritt, D. 1998, *ApJ*, 506, 686
- Valluri, M., & Merritt, D. 2000, *The Chaotic Universe, Proceedings of the Second ICRA Network Workshop, Advanced Series in Astrophysics and Cosmology*, vol.10, Edited by V. G. Gurzadyan and R. Ruffini, World Scientific, 2000, p.229, 229
- Vincent, R. A., & Ryden, B. S. 2005, *ApJ*, 623, 137
- Warren, M. S., Quinn, P. J., Salmon, J. K., & Zurek, W. H. 1992, *ApJ*, 399, 405

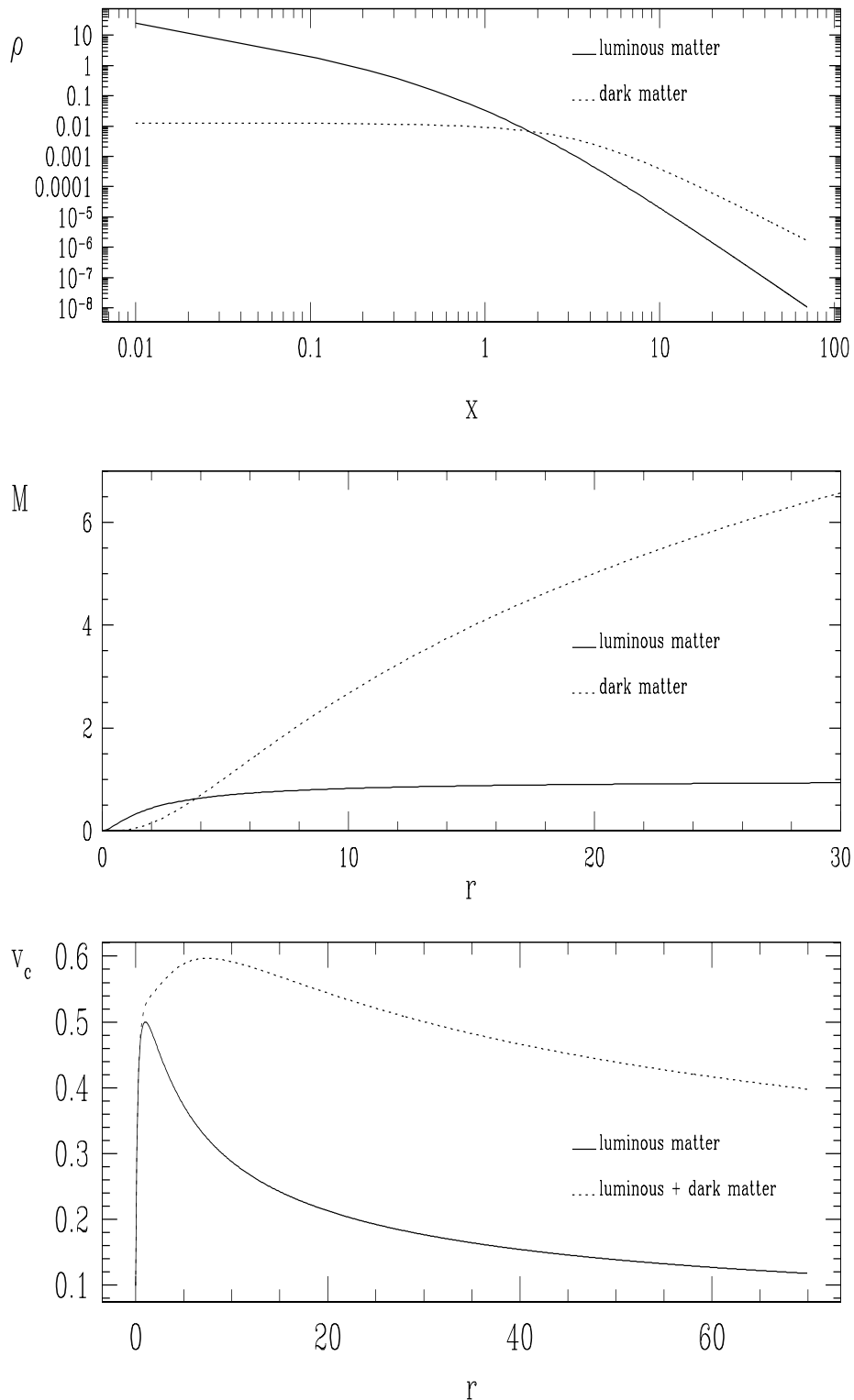


Fig. 1.— Top: long-axis density profiles of the luminous and dark matter components. Middle: mass enclosed within spheres of radius r in the case $a = b = c$. Bottom: circular velocity profiles in the spherical model, including both components (dashed line), and in a model without dark matter

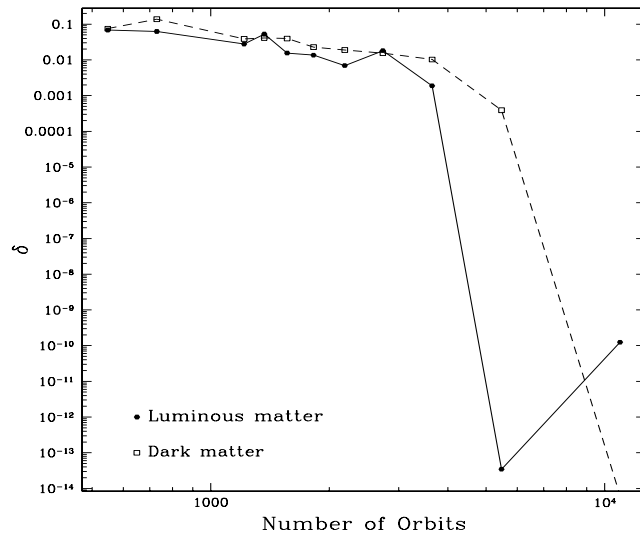
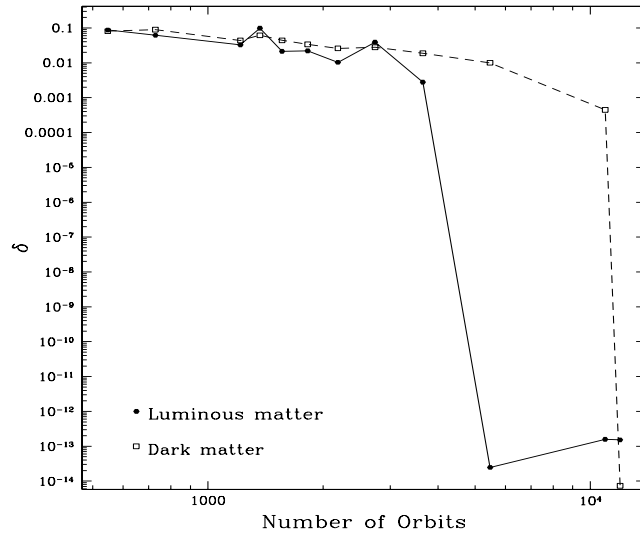
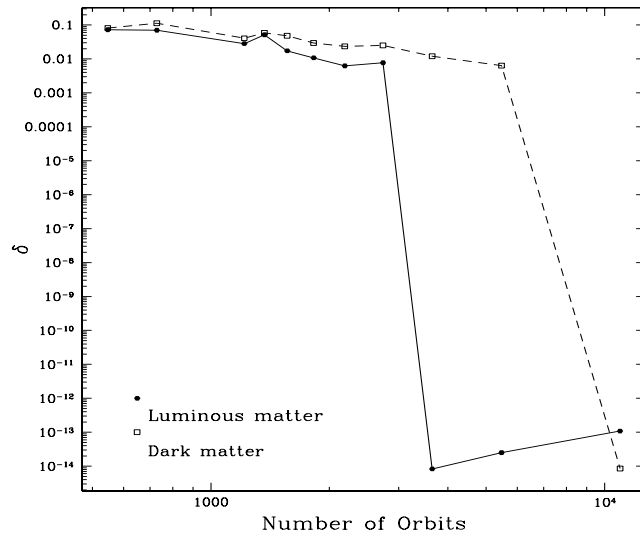


Fig. 2.— The rms deviation δ (equation 23) as a function of the number of orbits supplied to

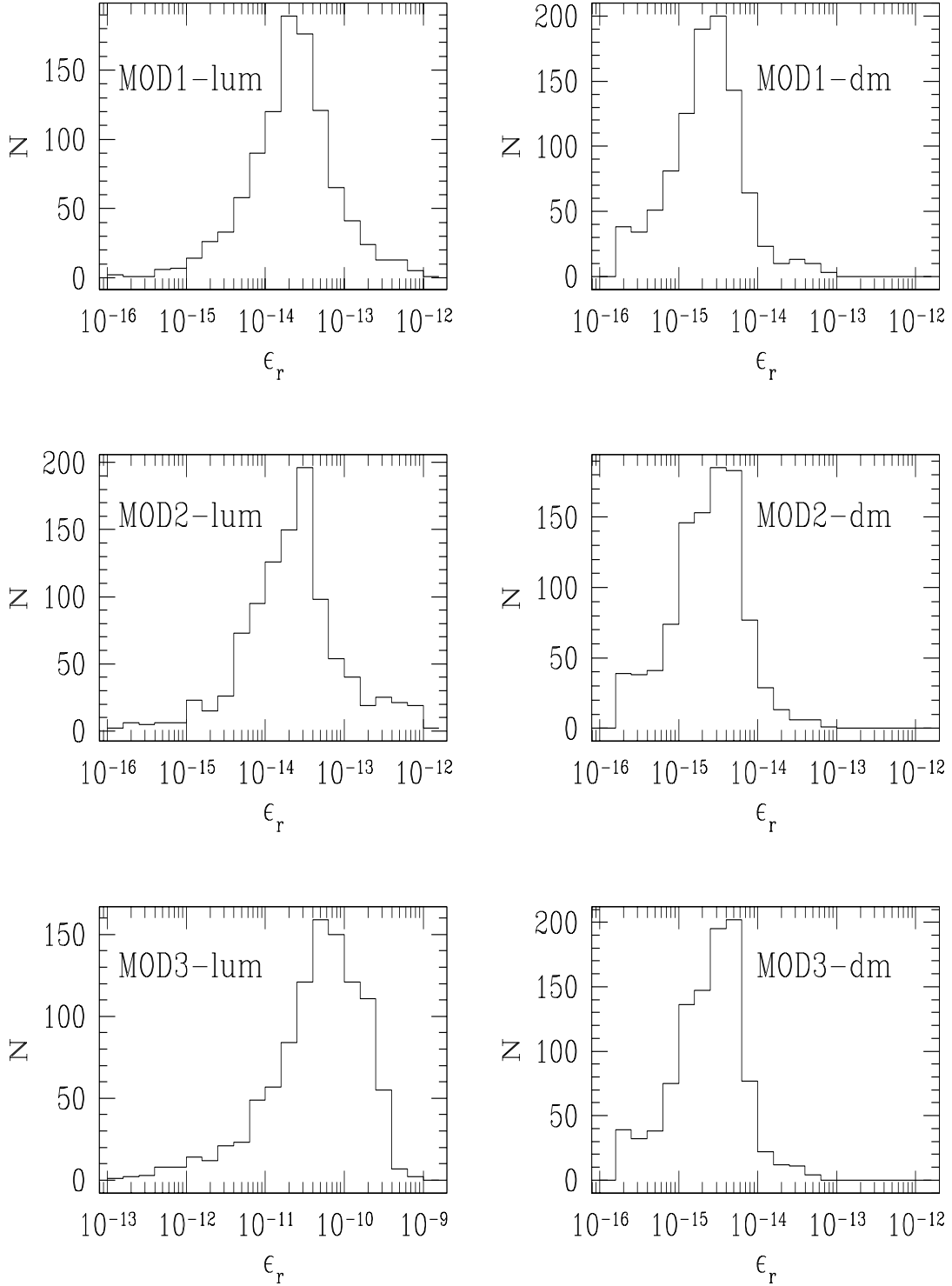


Fig. 3.— Histograms of the relative errors ϵ_r (see text). They refer to both the components grids of the three models analyzed and are calculated using the C_k quantities of the self-consistent solutions.

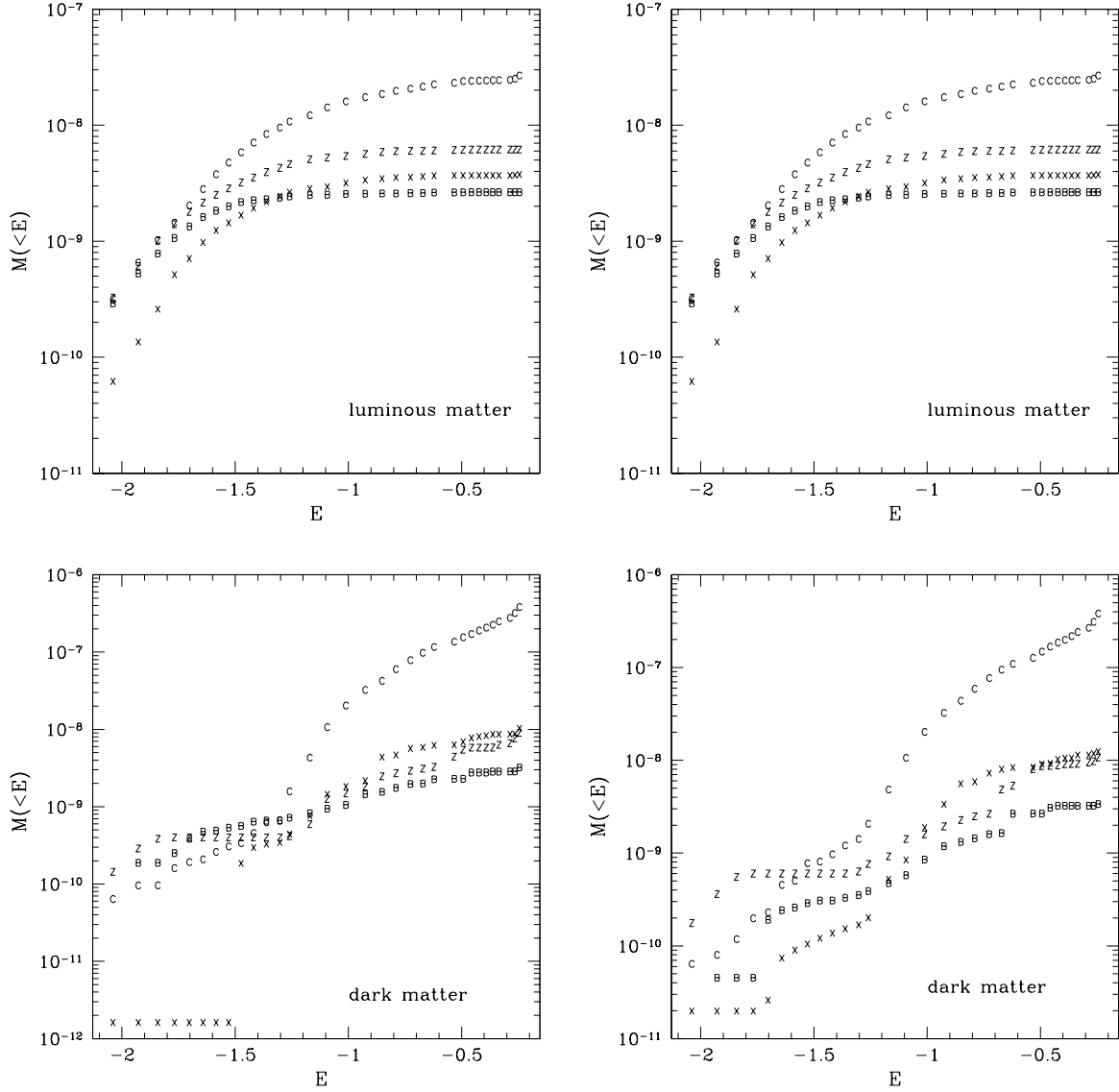


Fig. 4.— Cumulative, by mass, energy distributions of the various orbital families in the self-consistent solution of MOD1 (left column) and MOD1bis (right column). The symbols "B," "X," "Z," and "C" denote the mass contributed by box, x-tube, z-tube, and chaotic orbits, respectively.

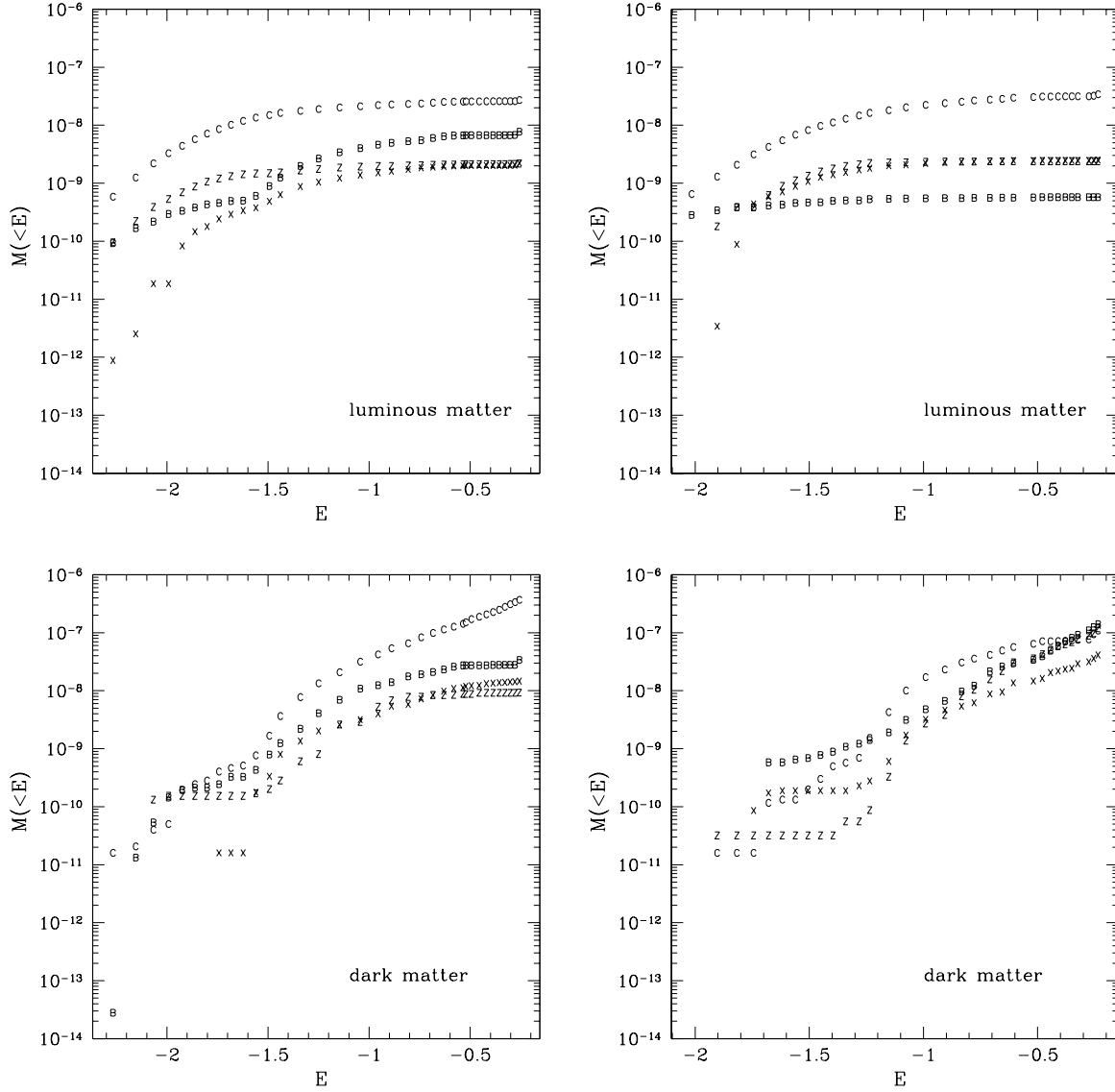


Fig. 5.— Cumulative, by mass, energy distributions of the various orbital families in the self-consistent solution of MOD2 (left column) and MOD3 (right column). The symbols "B," "X," "Z," and "C" denote the mass contributed by box, x-tube, z-tube, and chaotic orbits, respectively.

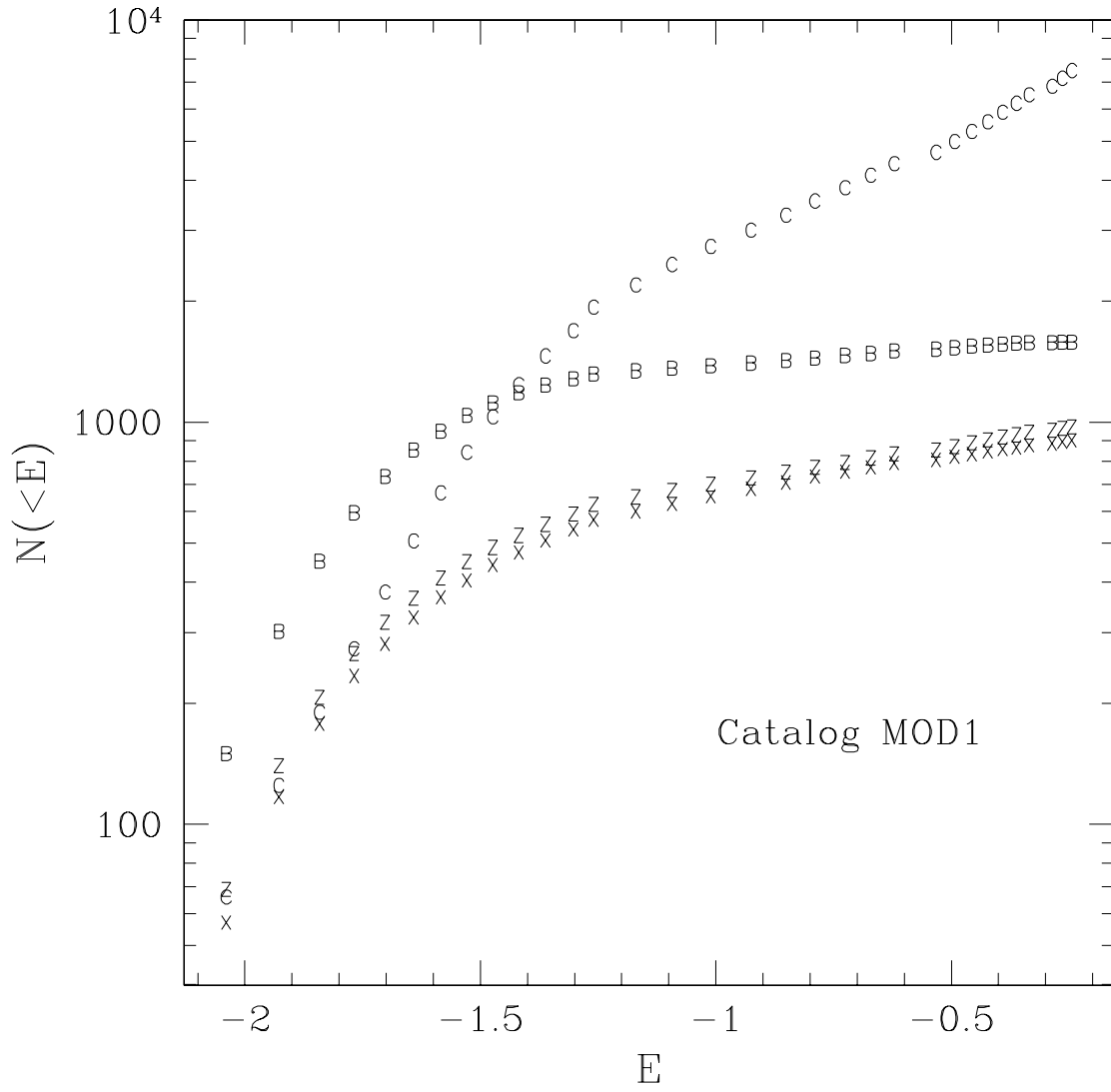


Fig. 6.— Cumulative, by number, energy distribution of the whole MOD1 orbital catalog. Symbols as in Fig. 4

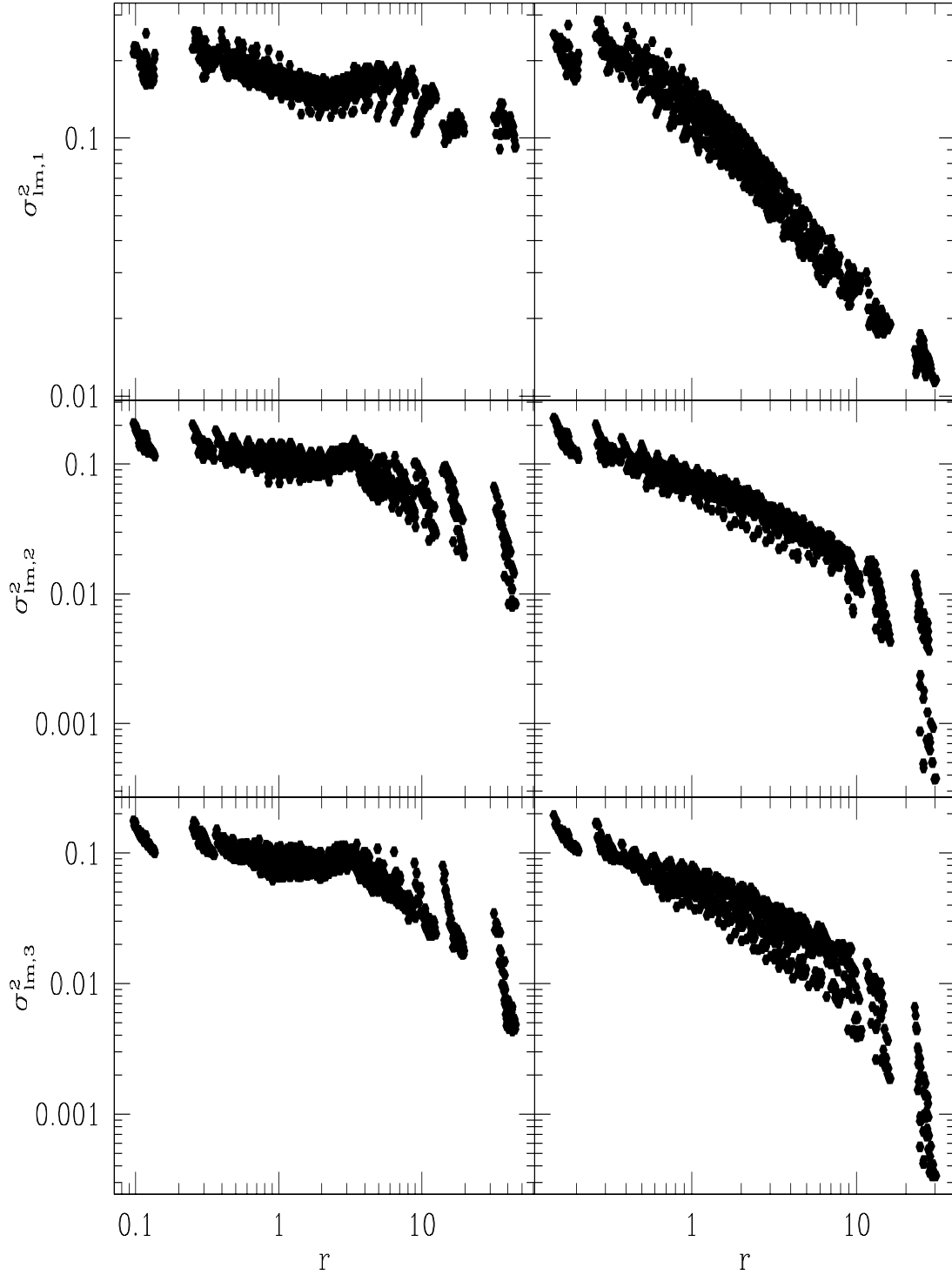


Fig. 7.— The stellar principal velocity dispersions $\sigma_{lum,l,i}^2$, $i = 1, 2, 3$ as functions of the distance from the centre in model MOD1 (left column) and in a model with the same luminous mass but without dark matter (right column).

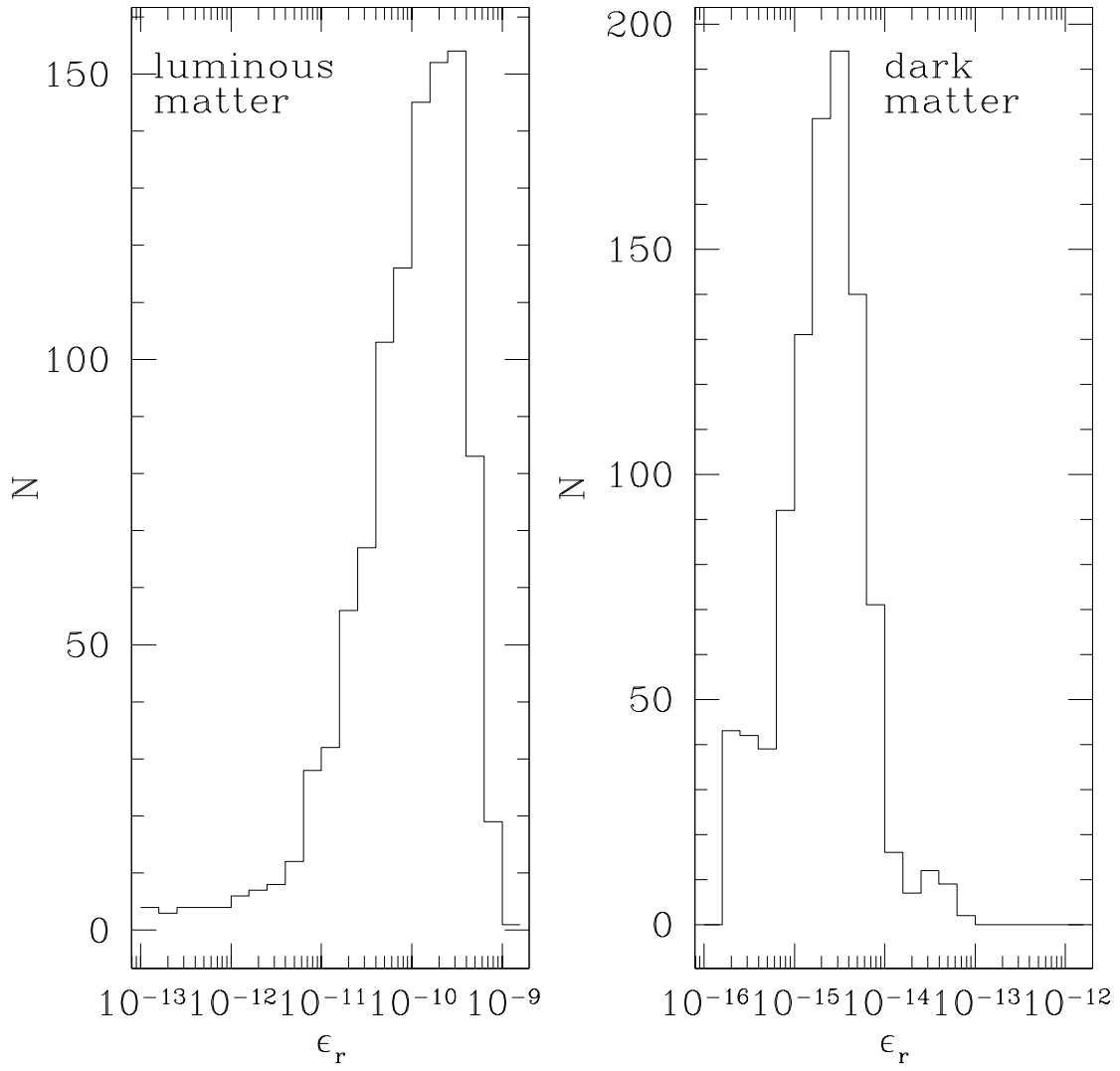


Fig. 8.— Histograms of the relative errors ϵ_r for MOD1bis, referring to the luminous and dark matter component, respectively.

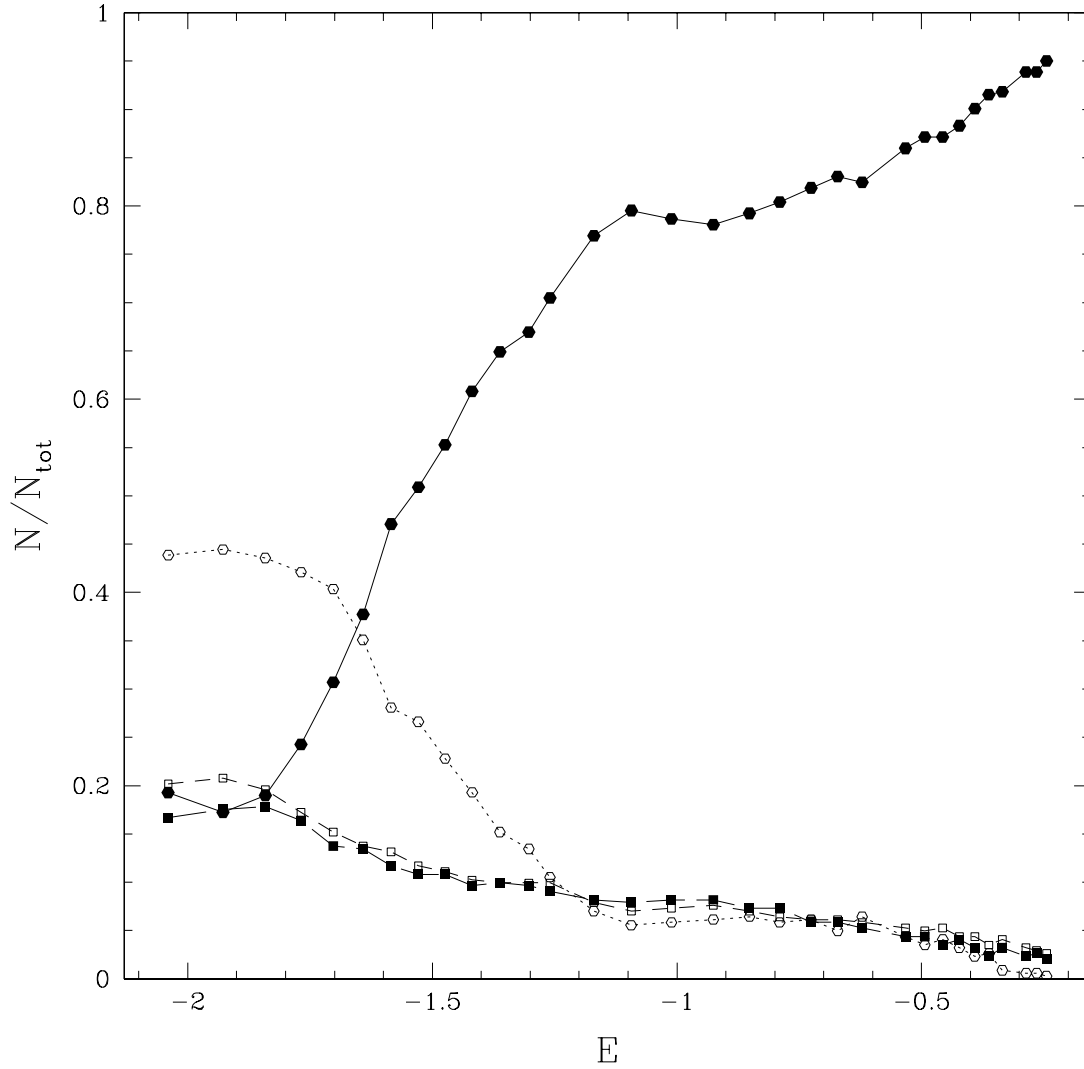


Fig. 9.— Fraction of different types of orbits in the full MOD1 orbital catalog vs energy. Full circles represent stochastic orbits; open circles are box-like orbits; open and full squares correspond to short and outer tube orbits respectively.

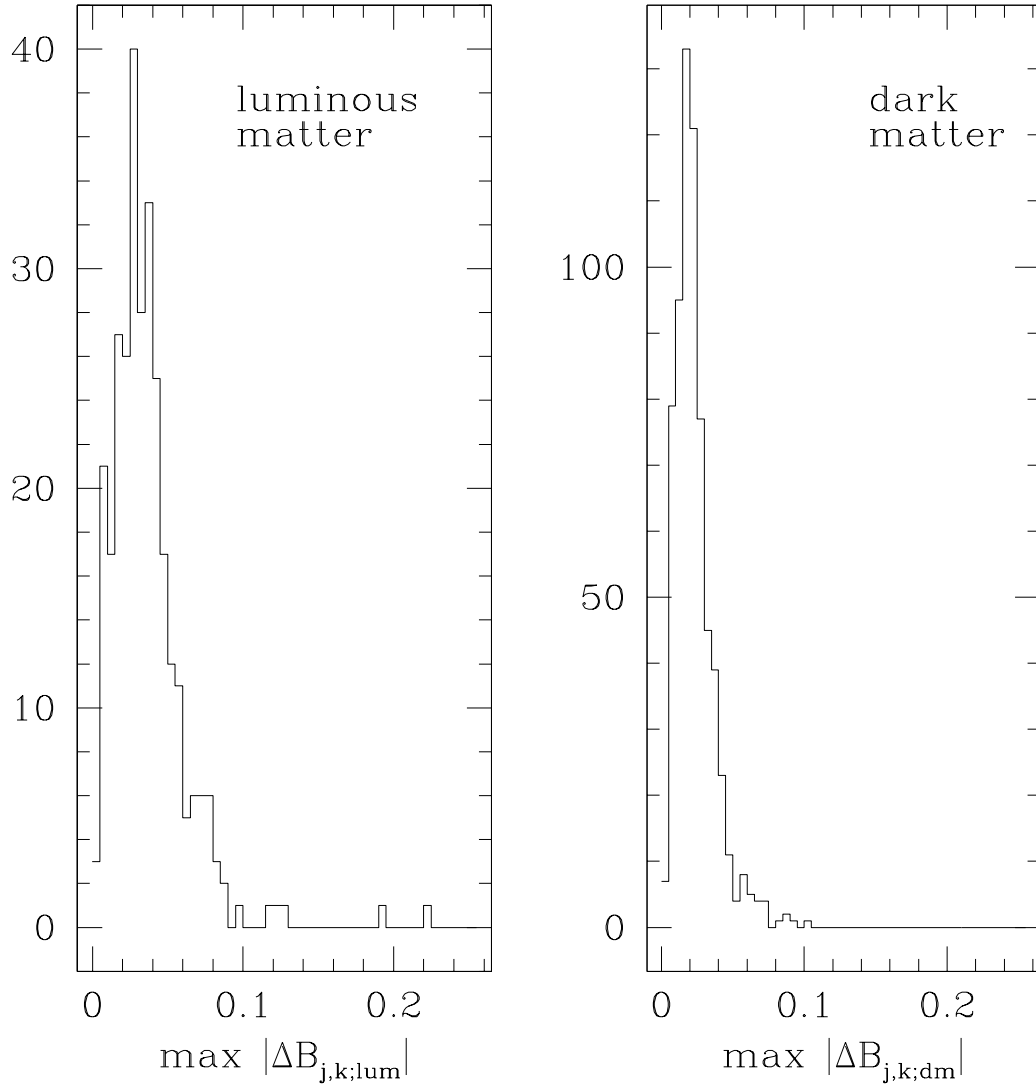


Fig. 10.— Histograms of the maximum $|\Delta B_{j,k}|$ for the stochastic orbits used in MOD1bis integrated once up to $5T_H$ and once up to $6T_H$.

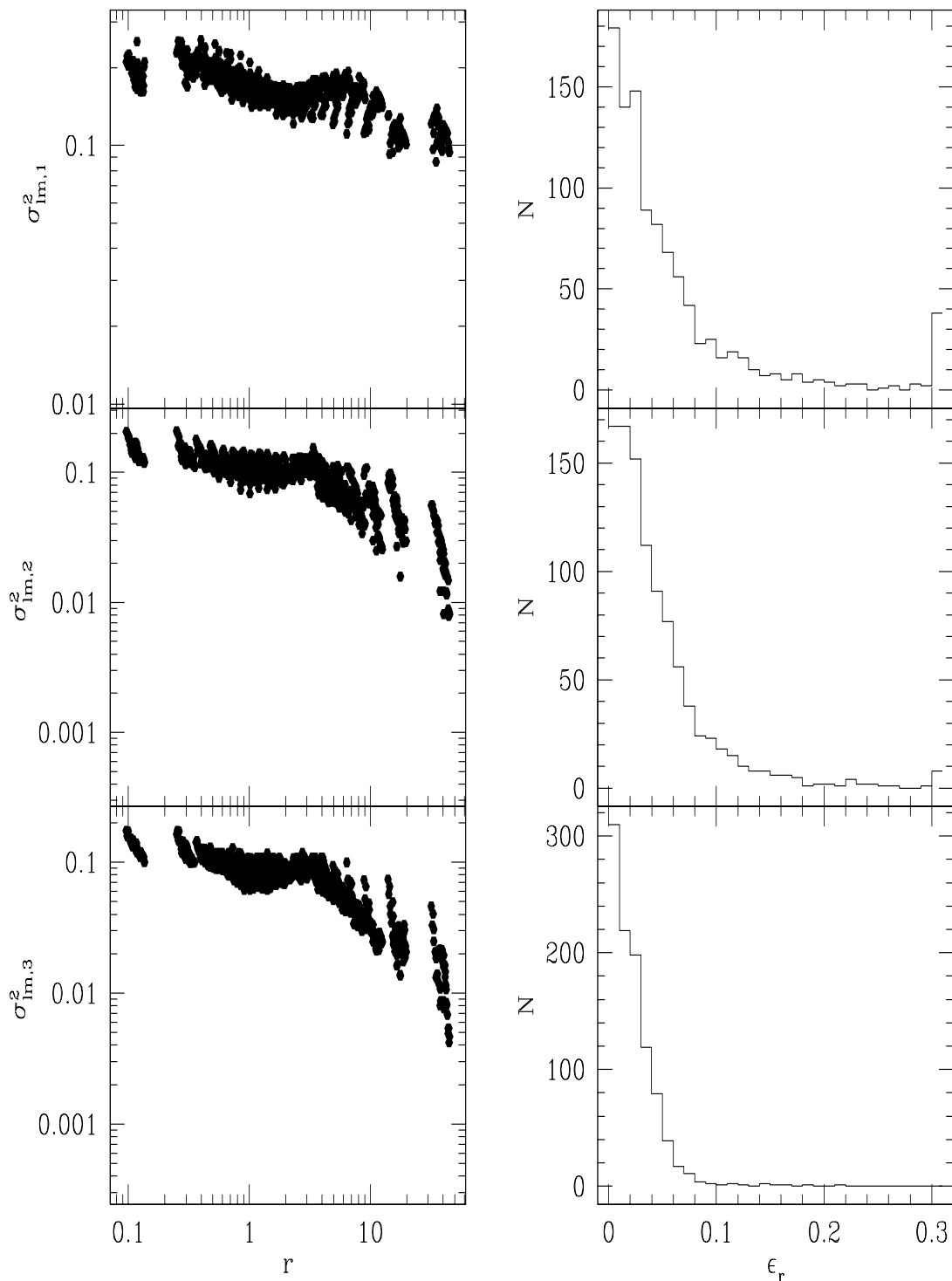


Fig. 11.— Left column: principal velocity dispersions for the luminous component, obtained with the self-consistent solution realized after having integrated orbits over $5T_H$ (MOD1bis). Right column: relative change in this quantity with respect to that obtained with the self-consistent solution after having integrated the orbits over $2T_H$.